# Clipped speckle autocorrelation metric for spot size characterization of focused beam on a diffuse target

**Yuanyang Li,[1,2,*] Jin Guo,[1] Lisheng Liu,[1] Tingfeng Wang,[1] Wei Tang,[1] and Zhenhua Jiang[1]**

[1]*State Key Laboratory of Laser Interaction with Matter, Changchun Institute of Optics, Fine Mechanics and Physics, Chinese Academy of Sciences, Changchun, Jilin 130033, China*
[2]*University of Chinese Academy of Sciences, Beijing 100039, China*
[*]*liyuanyang1108@sina.com*

**Abstract:** The clipped speckle autocorrelation (CSA) metric is proposed for estimating the laser beam energy concentration on a remote diffuse target in a laser beam projection system with feedback information. Using the second order statistics of the intensity distribution of the fully developed speckle and the relation of the autocorrelation functions for the clipped and unclipped speckles, we present the theoretical expression of this metric as a function of the normalized CSA function. The simulation technique based on the equivalence of the spatial average and the ensemble time average is provided. Based on this simulation technique, we analyze the influence of the surface roughness of the target on this metric and then show the influencing factors of the metric performance, for example the finite sample effect and aperture size of the observation system. Experimental results are illustrated to examine the capability of this metric and the correctness of the discussion about the metric performance.



**OCIS codes:** (030.6140) Speckle; (030.1670) Coherent optical effects; (140.3295) Laser beam characterization; (140.3460) Lasers.

## References and links

1. T. Yoshimura, M. Zhou, K. Yamahai, and Z. Liyan, "Optimum determination of speckle size to be used in electronic speckle pattern interferometry," Appl. Opt. **34**(1), 87–91 (1995).
2. S. E. Skipetrov, J. Peuser, R. Cerbino, P. Zakharov, B. Weber, and F. Scheffold, "Noise in laser speckle correlation and imaging techniques," Opt. Express **18**(14), 14519–14534 (2010).
3. D. V. Semenov, S. V. Miridonov, E. Nippolainen, and A. A. Kamshilin, "Statistical properties of dynamic speckles formed by a deflecting laser beam," Opt. Express **16**(2), 1238–1249 (2008).
4. J. C. Dainty, *Laser Speckle and Related Phenomena* (Springer, 1975).
5. P. Piatrou and M. Roggemann, "Beaconless stochastic parallel gradient descent laser beam control: numerical experiments," Appl. Opt. **46**(27), 6831–6842 (2007).
6. M. A. Vorontsov, G. W. Carhart, and J. C. Ricklin, "Adaptive phase-distortion correction based on parallel gradient-descent optimization," Opt. Lett. **22**(12), 907–909 (1997).
7. X. Lei, S. Wang, H. Yan, W. Liu, L. Dong, P. Yang, and B. Xu, "Double-deformable-mirror adaptive optics system for laser beam cleanup using blind optimization," Opt. Express **20**(20), 22143–22157 (2012).
8. T. Sawatari and A. C. Elek, "Image plane detection using laser speckle patterns," Appl. Opt. **12**(4), 881–883 (1973).
9. M. A. Vorontsov and G. W. Carhart, "Adaptive phase distortion correction in strong speckle-modulation conditions," Opt. Lett. **27**(24), 2155–2157 (2002).
10. D. Li, D. P. Kelly, and J. T. Sheridan, "Three-dimensional static speckle fields. Part I. Theory and numerical investigation," J. Opt. Soc. Am. A **28**(9), 1896–1903 (2011).
11. R. Barakat, "Clipped correlation functions of aperture integrated laser speckle," Appl. Opt. **25**(21), 3885–3888 (1986).
12. M. B. Priestley, *Spectral Analysis and Time Series* (Academic, 1981).
13. A. D. Ducharme, G. D. Boreman, and D. R. Snyder, "Effects of intensity thresholding on the power spectrum of laser speckle," Appl. Opt. **33**(13), 2715–2720 (1994).
14. H. M. Pedersen, "Theory of speckle-correlation measurements using nonlinear detectors," J. Opt. Soc. Am. A **1**(8), 850–855 (1984).

#232043 - $15.00 USD Received 8 Jan 2015; revised 28 Feb 2015; accepted 1 Mar 2015; published 12 Mar 2015

15. A. J. Lambert and D. Fraser, "Linear systems approach to simulation of optical diffraction," Appl. Opt. **37**(34), 7933–7939 (1998).
16. A. K. Fung and M. F. Chen, "Numerical simulation of scattering from simple and composite random surfaces," J. Opt. Soc. Am. A **2**(12), 2274–2284 (1985).
17. J. W. Goodman, *Statistical Optics* (John Wiley & Sons, 2000).

## 1. Introduction

When a diffuse target is illuminated with coherent, polarized light, the grain-like distribution of the reflected field is generated due to the interference of the fields reflected from different parts of the rough surface. The reflected field in this situation is called speckle field which has been studied in many papers. The speckle fields are widely applied because they may carry the information about the profile of the rough surface, for example by using the double scattered speckle image, or about the character of the illuminating beam in some certain conditions. And these information can be extracted by speckle interferometry [1], speckle photography [2], and many other methods [3, 4].

If the points on the rough surface of the diffuse target is delta-correlated and the RMS (root-mean-squared) roughness is relatively large (comparing to the wavelength), the surface property of the diffuse target do not affect the second order statistics of the speckle field. In this situation, the speckle field scattered by the very rough surface is generally called a fully developed one. The second order statistics of the fully developed speckle, which is mainly established by Goodman and many other scientists [4], is relatively simple than that of the undeveloped speckle and may have potential applications in engineering. Based on Goodman's theory, the average speckle size of the fully developed speckle is inversely proportional to the beam spot size on the rough surface. Hence the second order statistics of the speckle field can provide beam quality metrics for estimating the laser beam concentration on a remotely located diffuse target. For the beaconless laser beam projection system [5], a reliable beam quality metric is essential because the metric performance determines the final optimized result which an optimization algorithm, such as the stochastic parallel gradient descent (SPGD) technique, can reach. Having been widely used in the field of adaptive optics, the SPGD algorithm developed by Voronstov [6] belongs to a model free optimization algorithm and for this kind of algorithms, an appropriate metric for the model would take full advantage of the feedback signal and make the optimizing process faster and more stable. On the opposite, an inappropriate metric would result failure in optimization. In the laser projection application, the most widely used and simplest way to obtain the feedback of the beam concentration information is based on directly imaging the focusing spot on the target [5, 7]. But Sawatari and Elek [8] proposed that the enormous variation in the grain size of the speckle pattern would be a more accurate metric than the direct observation of the beam waist size. Based on their work, Voronstov and Carhart [9] introduce a beam quality metric by integrating the edge-indicator map of the speckle pattern, which is essentially a metric for grain size change. Cooperating with the SPGD algorithm, the wave front correction using this metric improved the beam concentration on an extended diffuse object.

In this paper, we propose a metric for estimating the beam energy concentration on a diffuse target. This beam quality metric is based on the spatial autocorrelation of the clipped speckle pattern. Since the speckle intensity distribution is generally assumed to be approximately ergodic in the space domain, spatial average is used instead of ensemble time average which brings enormous convenience for the calculation of speckle autocorrelation [10]. Besides, Barakat [11] built the one-to-one map between the unclipped and clipped speckle correlation function. Consequently, the clipped speckle autocorrelation (CSA) metric can be achieved based on these theories. Although the speckle metrics for beam energy concentration has been applied experimentally [9], the performance and restriction of this kind of metric are seldom discussed. Voronstov [9] proposed that the adaptive speckle-metric-based system can ideally reduce the focusing spot size to the point where there is only one speckle in the observation aperture. However, we will show that, due to the statistical property of the speckle pattern, the metric becomes unstable when the number of the speckles in the observation aperture is small. Hence, we will focus on the influence to the CSA metric

#232043 - $15.00 USD Received 8 Jan 2015; revised 28 Feb 2015; accepted 1 Mar 2015; published 12 Mar 2015

in this paper from the finite sample effect (due to small number of speckles in the aperture), observation system parameters and surface roughness of the target.

This paper is organized as follows: In Section 2, a revision of the theory of the speckle autocorrelation function is given and the basic idea of the CSA metric is translated. In Section 3, we discussed the simulation method for this CSA metric based system, and mainly based on the simulation result, the influences of the system parameters, the target character and the finite sample effect on the metric are discussed. The experimental result is shown in Section 4 where emphasis is mainly placed on the examination of the metric performance discussion. Finally, some concluding remarks are delivered in Section 5.

## 2. Clipped speckle autocorrelation metric for laser beam focusing

A schematic representation of a general laser beam projection system is illustrated in Fig. 1. Notice that we have given the two-way propagation path in an 'unfolded' manner for simplicity and clarity, and the transmitting propagation path is omitted here for it is not related to the main problem discussed in this section. The propagation path from a diffuse target to the receiving system is described as a whole optical system using an ABCD matrix. In the observation plane $\mathbf{r} = (x,y)$, the speckle distribution is obtained due to the random phase modulation of the laser beam in the diffuse target plane $\boldsymbol{\rho} = (\xi,\eta)$. The speckle field carries the information about the focusing spot dimension. We should use a function as a metric, like intensity autocorrelation function, to extract this information, and then process it with some techniques to make sure that it can be brought into play in practical applications.

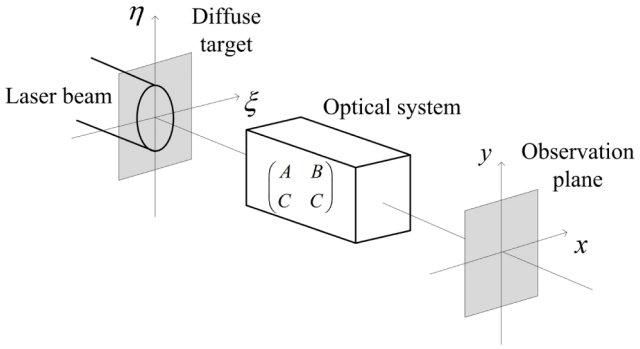


Fig. 1. An unfolded representation of the laser beam projection system

### *2.1. Preliminary*

In this subsection we give a brief review of the derivation of the speckle autocorrelation function. The main theory of this subject is mostly based on the work of Goodman [4], and we reintroduce it here for completeness. The laser beam is supposed to be quasi-monochromatic and linear polarized. The autocorrelation function $R(\mathbf{r}_1,\mathbf{r}_2)$ of the intensity distribution $I(\mathbf{r})$ is applied to character the speckle size as:

$$R(\mathbf{r}_1,\mathbf{r}_2) = \left\langle I(\mathbf{r}_1) I(\mathbf{r}_2) \right\rangle. \tag{1}$$

The angle brackets means taking the ensemble average over the realizations of the speckle pattern of different rough surfaces.

If the speckle is assumed to be fully developed, the real and imaginary part of the speckle field $U(\mathbf{r})$ in the observation plane are independent with respect to each other, thus this speckle field can be modeled by a circular complex Gaussian variable. Based on this fact, and applying the complex Gaussian moment theorem [12], the autocorrelation function $R(\mathbf{r}_1,\mathbf{r}_2)$ is given in a very simple form:

#232043 - $15.00 USD Received 8 Jan 2015; revised 28 Feb 2015; accepted 1 Mar 2015; published 12 Mar 2015

$$R(\mathbf{r}_1,\mathbf{r}_2)=\left\langle I(\mathbf{r}_1)\right\rangle\left\langle I(\mathbf{r}_2)\right\rangle+\left|J(\mathbf{r}_1,\mathbf{r}_2)\right|^2, \tag{2}$$

where $J(\mathbf{r}_1, \mathbf{r}_2)$ is defined as

$$J(\mathbf{r}_1,\mathbf{r}_2)=\left\langle U(\mathbf{r}_1)U^*(\mathbf{r}_2)\right\rangle. \tag{3}$$

The calculation of the intensity autocorrelation function $R(\mathbf{r}_1,\mathbf{r}_2)$ now reduces to the problem of getting the autocorrelation function of the speckle field $J(\mathbf{r}_1,\mathbf{r}_2)$ which is referred to as mutual coherence function (MCF) due to the same form in coherence theory [4]. For the reason that $J(\mathbf{r}_1,\mathbf{r}_2)$ is determined by the optical field $U(\mathbf{r})$, we need Huygens-Fresnel principle to calculate the optical field propagation from the diffuse target plane to the observation plane. The generalized Fresnel formula for ABCD systems is first derived by Collins as [10]:

$$U(\mathbf{r})=\frac{1}{j\lambda B}\int U_0(\boldsymbol{\rho})\exp\left[-\frac{jk}{2B}(A\rho^2-2\mathbf{r}\cdot\boldsymbol{\rho}+Dr^2)\right]\mathrm{d}^2\rho, \tag{4}$$

where $U_0(\boldsymbol{\rho})$ denotes the scattered field in the diffuse target plane in Fig. 1, and A, B and D are the elements of the ray matrix which represents the optical system. The symbol $k = 2\pi/\lambda$ is the wave number here and $\lambda$ is the wavelength. We do not consider the trivial case of $B = 0$, therefore Eq. (4) is sufficient for our purposes in this study. Substituting Eq. (4) into Eq. (3), we can obtain the relation of the MCFs in both target and observation planes:

$$\begin{aligned}J(\mathbf{r}_1,\mathbf{r}_2)=&\frac{1}{\lambda^2B^2}\exp\left[-\frac{jk}{2B}(r_1^2-r_2^2)\right]\int\mathrm{d}^2\rho_1\int\mathrm{d}^2\rho_2 J_0(\boldsymbol{\rho}_1,\boldsymbol{\rho}_2)\\&\times\exp\left\{-\frac{jk}{2B}\left[A(\rho_1^2-\rho_2^2)-2(\mathbf{r}_1\cdot\boldsymbol{\rho}_1-\mathbf{r}_2\cdot\boldsymbol{\rho}_2)\right]\right\},\end{aligned} \tag{5}$$

where $J_0(\boldsymbol{\rho}_1,\boldsymbol{\rho}_2)$ is the MCF in the diffuse target plane. If a function $P(\boldsymbol{\rho})$ is used to describe the amplitude distribution of the field in the diffuse target plane, the MCF $J_0(\boldsymbol{\rho}_1,\boldsymbol{\rho}_2)$ can be given as:

$$J_0(\boldsymbol{\rho}_1,\boldsymbol{\rho}_2)=\kappa P(\boldsymbol{\rho}_1)P^*(\boldsymbol{\rho}_2)\mu_0(\Delta\boldsymbol{\rho})\simeq\kappa\left|P(\boldsymbol{\rho}_1)\right|^2\mu_0(\Delta\boldsymbol{\rho}), \tag{6}$$

where $\Delta\boldsymbol{\rho} = \boldsymbol{\rho}_1-\boldsymbol{\rho}_2$, and $\kappa$ denotes the reflective coefficient. In Eq. (6), the function $\mu_0(\Delta\boldsymbol{\rho})$ is a complex coherence factor that is related to the reflected field in the $\boldsymbol{\rho} = (\xi,\eta)$ plane as suggested by Goodman [4]. Taking Eq. (6) into Eq. (5), we can finally obtain the MCF in the observation plane:

$$\begin{aligned}J(\mathbf{r}_1,\mathbf{r}_2)=&\frac{\kappa}{\lambda^2B^2}\exp\left[-\frac{jk}{2B}(r_1^2-r_2^2)\right]\int\mathrm{d}^2\rho_1\int\mathrm{d}^2\Delta\rho\left|P(\boldsymbol{\rho}_1)\right|^2\mu_0(\Delta\boldsymbol{\rho})\\&\times\exp\left\{-\frac{jk}{2B}\left[A(-2\boldsymbol{\rho}_1\cdot\Delta\boldsymbol{\rho}-\Delta\rho^2)-2(\mathbf{r}_1\cdot\boldsymbol{\rho}_1-\mathbf{r}_2\cdot\boldsymbol{\rho}_1-\mathbf{r}_2\cdot\Delta\boldsymbol{\rho})\right]\right\}.\end{aligned} \tag{7}$$

If the microstructure of the surface is so fine that it cannot be resolved by a lens the size of the observation region in the plane $\mathbf{r} = (x,y)$, the function $\mu_0(\Delta\boldsymbol{\rho})$ is supposed to be a $\delta$-function. And then Eq. (7) can be simplified as:

$$J(\Delta\mathbf{r})=\frac{\kappa}{\lambda^2B^2}\exp\left(-\frac{jk}{2B}\Delta r^2\right)\int\mathrm{d}^2\rho_1\left|P(\boldsymbol{\rho}_1)\right|^2\exp\left(\frac{jk}{B}\boldsymbol{\rho}_1\cdot\Delta\mathbf{r}\right), \tag{8}$$

where $\Delta\mathbf{r} = \mathbf{r}_1-\mathbf{r}_2$. Taking Eq. (8) into Eq. (2), we obtain the intensity autocorrelation for fully developed speckles:

#232043 - $15.00 USD Received 8 Jan 2015; revised 28 Feb 2015; accepted 1 Mar 2015; published 12 Mar 2015

$$R(\Delta\mathbf{r}) = \langle I \rangle^2 \left[ 1 + \left| \frac{\int |P(\boldsymbol{\rho})|^2 \exp\left( \frac{jk}{B} \boldsymbol{\rho} \cdot \Delta\mathbf{r} \right) \mathrm{d}^2 \rho}{\int |P(\boldsymbol{\rho})|^2 \, \mathrm{d}^2 \rho} \right|^2 \right]. \tag{9}$$

We write $\langle I \rangle$ short for $\langle I(\mathbf{r}) \rangle$ since it is not dependent on the position **r**. Equation (9) can be found in many papers [4, 10] for fully developed speckles. This relation clearly shows that the autocorrelation length of the intensity distribution is inversely proportional to the dimension of the focusing spot described by the function $P(\boldsymbol{\rho})$. Next, we should put forward a proper metric to extract the useful information from the intensity autocorrelation function of the speckles.

*2.2. Clipped speckle autocorrelation merit for laser beam focusing*

Autocorrelation is a time consuming process for very large amount of data, for example the process for the fully recorded laser speckle distribution, because the analog-to-digital converter, the full-bit registers and multiplexers should be used [13]. If we clip the fully recorded speckle data to binary data, many resources can be saved and the speed of the autocorrelation calculation can be increased noticeably. Another advantage of the clipping process is that the background noise for speckle recording would be eliminated if the background noise is small compared to the threshold of the speckle signal. Even if some of the information of the speckle distribution is lost in the clipping procedure, the properties of intensity autocorrelation calculation are not much affected as we illustrated below.

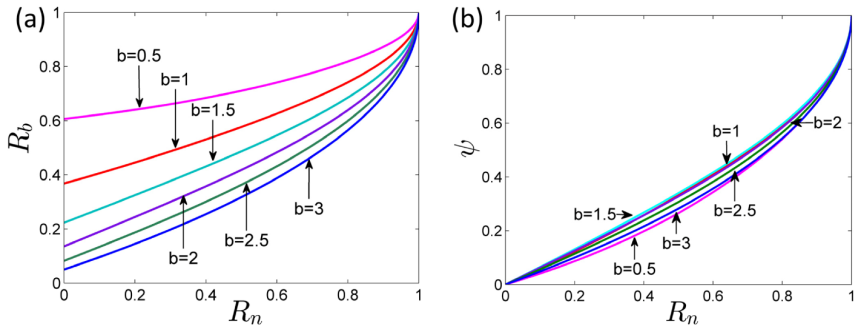


Fig. 2. (a) The clipped autocorrelation function $R_b(\Delta\mathbf{r})$ changes against the continuous normalized autocorrelation function $R_n(\Delta\mathbf{r})$ when the threshold parameter $b$ has the values from 0.5 to 3. (b) The relation of the function $R_n(\Delta\mathbf{r})$ and unbiased version of the clipped autocorrelation function $\psi(\Delta\mathbf{r})$.

We subtract the bias $\langle I(\mathbf{r}) \rangle$ out of the autocorrelation function $R(\Delta\mathbf{r})$ and then normalize it, so we get a normalized autocorrelation function $R_n(\Delta\mathbf{r})$. The relation of the clipped autocorrelation function $R_b(\Delta\mathbf{r})$ and the continuous normalized autocorrelation function $R_n(\Delta\mathbf{r})$ has been developed by Barakat [11]:

$$R_b(\Delta\mathbf{r}) \cong \exp(-b) \left\{ 1 + b^2 \sum_{n=1}^{\infty} \frac{\left[ L_{n-1}^{(1)}(b) \right]^2}{n^2} \left[ R_n(\Delta\mathbf{r}) \right]^n \right\}. \tag{10}$$

The parameter $b$ is defined as the threshold of the clipping procedure. If $I(\mathbf{r}) \geq b \langle I(\mathbf{r}) \rangle$, the value of the intensity is set to be 1, and the value of the speckle image is set to be 0 for $I(\mathbf{r}) < b \langle I(\mathbf{r}) \rangle$. The function $L_n^{(a)}$ is the associated Laguerre polynomial. If the value of the

#232043 - $15.00 USD Received 8 Jan 2015; revised 28 Feb 2015; accepted 1 Mar 2015; published 12 Mar 2015

normalized continuous autocorrelation $R_n(\Delta\mathbf{r})$ is given in the range of 0 to 1, the relation of $R_n(\Delta\mathbf{r})$ and $R_b(\Delta\mathbf{r})$ is illustrated in Fig. 2(a) as it suggested by Eq. (10). The clipping process introduces a bias to the autocorrelation function. This bias which equals to exp(-$b$) is determined by the threshold parameter $b$. One of important conclusions shown by Fig. 4(a) is that Eq. (10) is a monotone increasing function. The bijection of $R_n(\Delta\mathbf{r})$ and $R_b(\Delta\mathbf{r})$ means that $R_b(\Delta\mathbf{r})$ is a function of $R_n(\Delta\mathbf{r})$ only if threshold $b$ is given. In the practical applications, we usually obtain the $R_b(\Delta\mathbf{r})$ first, and then find the value of $R_n(\Delta\mathbf{r})$ with the relation between them. However, representing $R_n(\Delta\mathbf{r})$ with $R_b(\Delta\mathbf{r})$ is difficult for the closed form of Eq. (10) seems to be impossible [14]. In order to find an another way to take the place of Eq. (10), we introduce an unbiased version of the clipped autocorrelation function $R_b(\Delta\mathbf{r})$:

$$\psi(\Delta\mathbf{r}) = \frac{R_b(\Delta\mathbf{r}) - \exp(-b)}{\max\{R_b(\Delta\mathbf{r}) - \exp(-b)\}}. \tag{11}$$

The relation of $\psi(\Delta\mathbf{r})$ and $R_n(\Delta\mathbf{r})$ is shown in Fig. 2(b). It is interesting to notice that the curves of $b$ = 1, 1.5 and 2 are nearly superposed together, which gives us a chance to fit the curves with *one* simple formula. The mostly used threshold for practice is consistent with this range of $b$, for small $b$ cannot eliminate the background noise completely while large $b$ value makes the useful information run off. The superposition of the three curves in Fig. 4(b) also suggests that the clipping process do not introduce or eliminate much useful information of the clipped autocorrelation function no matter what the value of $b$ is in the range of 1 to 2. In this range of $b$, we use polynomials to fit the curves as:

$$R_n(\Delta\mathbf{r}) = \sum_{i=0}^{m} a_i [\psi(\Delta\mathbf{r})]^i. \tag{12}$$

The data for the curve fitting is obtained as follows: We sample the values of $b$ from the range of 1 to 2 with even spaces; and then calculate the values of $\psi(\Delta\mathbf{r})$ for these sampled values of $b$ using Eqs. (10) and (11); finally we take the average of $\psi(\Delta\mathbf{r})$ for different $b$ values and use this average to do the curve fitting according to Eq. (12). The curve fitting result is shown in Table 1. As the table shown, we fit this curve with the polynomials of maximum order 5.

**Table 1. Curve fitting result of Eq. (12)**

| Coefficients | $a_0$ | $a_1$ | $a_2$ | $a_3$ | $a_4$ | $a_5$ |
|---|---|---|---|---|---|---|
| Fitting result | 1.163e-4 | 1.576 | –0.1804 | –0.133 | –0.5253 | 0.2628 |

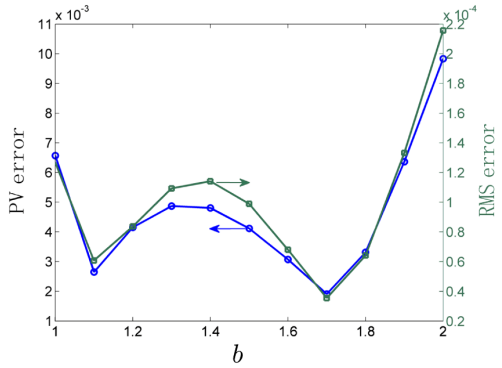


Fig. 3. Error analysis for taking the place of curves in Fig. 2(b) by the fitting result Eq. (12) when the threshold parameter $b$ is in the range of 1 to 2. PV error (left vertical axis) and RMS error (right vertical axis) are both given.

The error of taking the place of the exact curve in Fig. 4(b) with the fitting curve denoted by Eq. (12) is given in Fig. 3. The PV (peak-to-valley) error is defined as the maximum difference between the exact curve and the fitting curve, and the RMS error describes the root

#232043 - $15.00 USD Received 8 Jan 2015; revised 28 Feb 2015; accepted 1 Mar 2015; published 12 Mar 2015

of the squared sum of this difference. Figure 3 shows that the PV error is almost fifty times greater than the RMS error whatever the threshold parameter $b$ is in the range of 1 to 2. The RMS error can represent the global difference between the exact curve and the fitting curve, and the PV error reveals this point locally. In Fig. 3, the RMS error is small for all the possible $b$ values, which means that the fitting curve never departs greatly from the exact curves from the global point, and this is what we have demonstrated in Fig. 2(b). The maximum PV error, which is about 0.01, occurs when $b = 2$. For the metric we are going to discuss next, this PV error is not very noticeable or even submerges in the errors caused by the other effects, thus we can use Eq. (12) with much confidence. Using Eq. (12), it becomes much convenient to derive the CSA metric for laser beam focusing.

Since we are dealing with the laser beam focusing problems, the intensity distribution in the diffuse target plane should be Gaussian, and the amplitude function $P(\boldsymbol{\rho})$ of the beam is set to be:

$$P(\boldsymbol{\rho}) = \exp\left(-\frac{\rho^2}{\omega_0^2}\right), \tag{13}$$

where $\omega_0$ is the focusing spot radius of the laser beam in the target plane. We intentionally set the amplitude of the function $P(\boldsymbol{\rho})$ to be unit value because this amplitude should be eliminated by the normalization process. Taking Eq. (13) into Eq. (9), the normalized intensity autocorrelation function $R_n(\Delta\mathbf{r})$ is calculated by:

$$R_n(\Delta\mathbf{r}) = \frac{R(\Delta\mathbf{r})}{\langle I(\mathbf{r})\rangle^2} - 1 = \exp\left(-\frac{\pi^2\omega_0^2}{\lambda^2 B^2}|\Delta\mathbf{r}|^2\right). \tag{14}$$

Using Eq. (14), we can define a metric for laser beam focusing as:

$$M_e = |\Delta\mathbf{r}| = \frac{\lambda B}{\pi\omega_0}\left[\ln\left(\frac{1}{R_n(\Delta\mathbf{r})}\right)\right]^{1/2}. \tag{15}$$

This metric is defined as the length of the lag for a particular value of the autocorrelation function. Since the clipped speckle is used, the $R_n(\Delta\mathbf{r})$ is substituted by Eq. (12) and the CSA metric can be defined as:

$$M_e = \frac{\lambda B}{\pi\omega_0}\left[-\ln\sum_{i=0}^{m} a_i[\psi(\Delta\mathbf{r})]^i\right]^{1/2}. \tag{16}$$

Remember that Eq. (16) can be available only when the threshold parameter $b$ is in the range of 1 to 2. Once we have calculated the CSA function $\psi(\Delta\mathbf{r})$ from the raw data of CCD detector, the metric $M_e$ can be calculated to character the relative lateral size of the laser beam focusing spot due to the inversely proportional relationship between $M_e$ and $\omega_0$. Many factors may affect the accuracy of this metric: The property of the surface of the diffuse target may lead an unwished-for error, when the surface is not rough enough for a fully-developed speckle calculation; the accuracy of this metric also deeply depends on the sampling condition, such as the sampling number and the aperture size of the observation system. In the next section, we are going to focus on the accuracy and the limitations of the CSA metric based on the simulation results.

## 3. Simulations and discussions for the clipped speckle autocorrelation metric

In this section, we will show the simulations of the CSA process and give some discussions concerning the metric in laser beam focusing. At first, notice that the observation system is represented by an ABCD matrix in Fig. 1 for simplicity, and now we are going to give a detail configuration of the observation system. As shown in Fig. 4, the observation system for the

#232043 - $15.00 USD Received 8 Jan 2015; revised 28 Feb 2015; accepted 1 Mar 2015; published 12 Mar 2015

laser projection system is mainly composed of three parts: an intermediate plane, an observation lens and a detector. The intermediate plane does not really exit because it is introduced only for convenience. The observation lens is used for imaging the speckle distribution and the image is recorded by the detector. The speckle distribution imaged by the observation lens is not in the diffuse target plane but the intermediate plane, which means that the detected speckle image is the speckle distribution after the field propagates a distance $z_1$ from the target. And then we denote the distances from intermediate plane to the lens aperture as $z_2$ and from the lens to the detector as $z_3$.

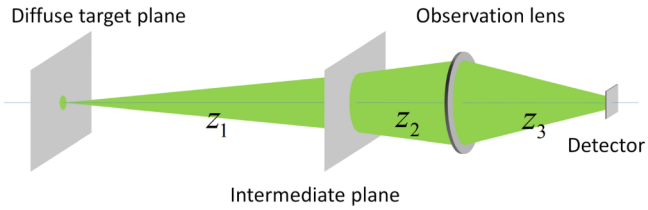


Fig. 4. Detail configuration of the observation system

The intermediate plane and the detector are conjugate planes for the observation lens. Using the multiplication property of the ray matrix, we have:

$$\begin{pmatrix} A_{im} & B_{im} \\ C_{im} & D_{im} \end{pmatrix} = \begin{pmatrix} 1 & z_3 \\ 0 & 1 \end{pmatrix} \begin{pmatrix} 1 & 0 \\ -1/f & 1 \end{pmatrix} \begin{pmatrix} 1 & z_2 \\ 0 & 1 \end{pmatrix}. \tag{17}$$

The parameter $f$ is the focal length of the observation lens. The conjugate property of intermediate plane and the detector makes the matrix element $B_{im}$ have a zero value. In this situation, the element $A_{im}$ stands for the magnifying power of the image system. Considering these relations, we have:

$$z_2 = f\left(1 - \frac{1}{A_{im}}\right), \tag{18a}$$

$$z_3 = f(1 - A_{im}). \tag{18b}$$

We treat the magnifying power $A_{im}$ as a known parameter because the intermediate plane for speckle imaging is free to choose, and in the practical situations, we should choose a value of $A_{im}$ appropriate for the size and resolving power of the detector. Combined with the speckle field propagation distance $z_1$ from the diffuse target, the whole optical path for focusing spot observation can be calculated by:

$$\begin{pmatrix} A & B \\ C & D \end{pmatrix} = \begin{pmatrix} 1 & z_3 \\ 0 & 1 \end{pmatrix} \begin{pmatrix} 1 & 0 \\ -1/f & 1 \end{pmatrix} \begin{pmatrix} 1 & z_2 \\ 0 & 1 \end{pmatrix} \begin{pmatrix} 1 & z_1 \\ 0 & 1 \end{pmatrix}. \tag{19}$$

According to Eq. (18) and Eq. (19), the results of the multiplication demonstrate that $B = A_{im}z_1$, $A = A_{im}$ and $C = -1/f$, and the parameter $D$ can be calculated by $AD\text{-}BC = 1$. The speckle field on the detector can be simulated by the Collins formula after obtaining the elements of this ABCD matrix.

Another important parameter, which we may encounter during applying the model in Fig. 4, is the area of the speckle field imaged on the detector. If the intermediate plane moves closer to the target plane, the area of the speckle field imaged on the detector would become smaller. This area is mainly determined by the aperture of the observation lens and the location of the intermediate plane. The aperture diameter of the observation lens is known as $\phi$, and then the diameter $\phi_{eff}$ of the area where the speckle field in the intermediate plane can be imaged by the lens is calculated according to the geometry in Fig. 4 as:

#232043 - $15.00 USD Received 8 Jan 2015; revised 28 Feb 2015; accepted 1 Mar 2015; published 12 Mar 2015

$$\phi_{eff} = \frac{\phi_{imag}}{|A_{im}|} = \frac{A_{im} z_1 \phi}{A_{im} z_1 + f(A_{im} - 1)}, \tag{20}$$

where $\phi_{imag}$ is the image size of the speckle on the detector which is $|A_{im}|$ times smaller than $\phi_{eff}$. The parameters of the observation system discussed above are preparations for the simulation of the CSA metric analysis.

*3.1 Numerical simulation method and parameter selections*

The numerical simulation method used in this paper is introduced in this subsection. In order to generate the speckle intensity in the detector plane, we should pay attention to three main issues, which are the simulations of the field propagation in the optical systems, of the diffuse target plane and of the intensity autocorrelation algorithm. We are going to introduce our simulation method from these three aspects.

For field propagation problem, we use the one step fast Fourier transform (FFT) method. The basic theory of this simulation algorithm is the Collins formula Eq. (4), but some adjustments are needed to make the Collins formula suited for the Fourier transform, and the detail description of this change can be found in [15]. Angular spectrum method is also widely used in the field propagation issue, but it is not appropriate for this speckle generation problem [10]. The angular spectrum algorithm needs a FFT and an inverse FFT. The first FFT will result a distorted numerical result because the bandwidth of the input speckle field is generally too broad for the finite sample area. Then the second inverse FFT will give a very noisy result. In the simulation, we use a square matrix of dimension $N \times N$ to describe the input and output field. In the simulations in this paper, we set $N = 1024$, and the sampling interval in the input plane is set to be 70 μm.

The way to simulate a diffuse target is important for our discussion. Unlike the other literatures [10], we do not simply use a pseudorandom number generator to generate uniformly distributed phase values over the range of 0 to $2\pi$, because the influence of the diffuse target property cannot be considered under this model. In this paper, we use a model mainly derived from the concept of digital filtering, in which a desired random profile can be simulated by the convolution of a set of filter weight and a sequence of independent Gaussian random variables. More details about this theory can be found in [16], and we use the main conclusion of this work directly:

$$H_{surf}(\xi,\eta) = FFT^{-1}\left[\sqrt{FFT\left[\Omega(\xi,\eta)\right]} FFT\left[X(\xi,\eta)\right]\right], \tag{21}$$

where $H_{surf}(\xi,\eta)$ is the discrete model of the random surface of the diffuse target; $X(\xi,\eta)$ denotes the independent standard Gaussian random variables at the point of $(\xi,\eta)$ while $\Omega(\xi,\eta)$ is the autocorrelation function of the rough surface. The symbols $FFT$ and $FFT^{-1}$ mean the fast Fourier transform algorithm and its inverse respectively. If we assume that the correlation function of the rough surface is Gaussian and that the root-mean-square (RMS) height is denoted by $h_{rms}$, the function $\Omega(\xi,\eta)$ can be write by:

$$\Omega(\xi,\eta) = h_{rms}^2 \exp\left(-\frac{\xi^2 + \eta^2}{l_c^2}\right). \tag{22}$$

The parameter $l_c$ in Eq. (22) is the autocorrelation length of the surface height. We use this simple model of the scatter effect from a diffuse target, and then the scatter field is that:

$$U_0(\xi,\eta) = P(\xi,\eta) \exp\left[ikH_{surf}(\xi,\eta)\right], \tag{23}$$

where $P(\xi,\eta)$ is the amplitude distribution of the scattering field as we mentioned in Eq. (13). Taking Eq. (23) into the field propagation algorithm, the speckle intensity distribution can be obtained in the observation plane or the detector plane. The parameters $h_{rms}$ and $l_c$ can be free

#232043 - $15.00 USD Received 8 Jan 2015; revised 28 Feb 2015; accepted 1 Mar 2015; published 12 Mar 2015

to choose in this model, but the theory in Section 2 is only available for the fully developed speckle field, viz., $h_{rms}$ is relatively large and $l_c$ relatively small. In the next subsection, the discussion will be focused on the extent where the values of $h_{rms}$ and $l_c$ are available for this theory.

After obtaining the speckle field in the observation plane, the CSA function can be derived using a certain algorithm. The ensemble average in Eq. (1) is replaced by the spatial average in the autocorrelation algorithm. This process is accurate enough for sufficient long ergodic data sequences. The specific algorithm can be a FFT method which based on the Wiener-Khinchin theorem [17] or a shift-summation method (like the built-in function "normxcorr2" in Matlab) [10]. The criterion to choose what algorithm is the speed of each method in practical engineering. Notice that the distribution of the speckle image is isotropic and it is the length of autocorrelation function width that we are really interested, thus we can only calculate one orientation of shifts in the shift-summation method. This procedure could save at least half of the time in this algorithm. The realism of the autocorrelation algorithms is not very relevant to our paper, so we do not give further discussions for this issue.

We now give some simulations of the intensity autocorrelation of the clipped speckle. If there is no specific explanation, all the simulations in the next sections use the parameters delivered here. The parameters of the observation systems can be given as: $z_1$ = 8000 mm, $A_{im}$ = –0.1, $\phi$ = 76.5 mm and $\lambda$ = 0.532 μm. The parameters of the diffuse target is chosen to be $h_{rms}$ = 1 $\lambda$ and $l_c$ = 12.5 μm, which means the target is very rough and the speckle distribution is fully developed. The diameter of the speckle image area is calculated to be 60 mm according to Eq. (20). The simulation result of the clipped speckle distribution is shown in Fig. 5(a), 5(b) and 5(c) when the focusing spot radius $\omega_0$ is 1 mm, 2 mm and 3 mm respectively. The threshold parameter $b$ is chosen to be 1 here. Figure 5(d) illustrates the results of CSA function $\psi(\Delta\mathbf{r})$ of the different speckle distributions in Fig. 5(a), 5(b) and 5(c). We can find that the simulation results are consistent with the theoretical results calculated by Eq. (10) and (11) well. Therefore, the simulation methods we have given in this section are accurate enough for discussions of the CSA metric.

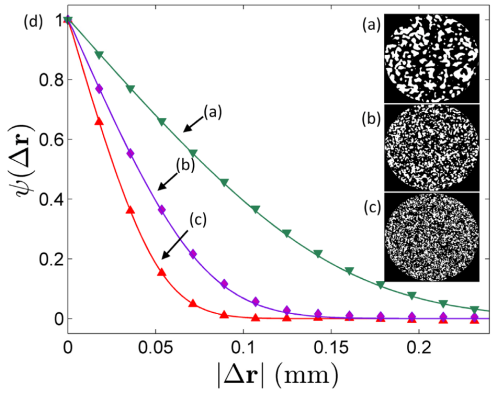


Fig. 5. The speckle intensity distributions are given in (a), (b) and (c) for the focusing spot size of 1 mm, 2 mm and 3 mm, respectively. The CSA functions $\psi(\Delta\mathbf{r})$ calculated by the simulation method are compared with the theoretical ones in (d). Solid lines are theoretical results and markers stand for the numerical ones.

### *3.3 Influence of surface roughness on the clipped speckle autocorrelation*

The metric is derived from the assumption that the speckles are fully developed. If the surface roughness is not very great, the autocorrelation of the clipped speckle would deviate from Eq. (10) and (12), which would cause error of the metric. Hence the influence of the surface roughness should be discussed here.

#232043 - $15.00 USD Received 8 Jan 2015; revised 28 Feb 2015; accepted 1 Mar 2015; published 12 Mar 2015

Since we are now dealing with the laser beam focusing problem for a long propagation distance which is the subject of this paper, the size of the focusing spot is naturally much smaller than the propagation distance. Using this fact, we can simplify Eq. (7) with the method in [4] as:

$$J(\mathbf{r}_1,\mathbf{r}_2)\approx K(\Delta r)G(\mathbf{r})\int\left|P(\boldsymbol{\rho})\right|^2\exp\left(\frac{jk}{B}\boldsymbol{\rho}\cdot\Delta\mathbf{r}\right)\mathrm{d}^2\rho=J(\mathbf{r},\Delta\mathbf{r}),\tag{24}$$

where,

$$\begin{aligned}K(\Delta r)&=-\frac{\kappa}{\lambda^2B^2}\exp\left(-\frac{jk}{2B}\Delta r^2\right);\\ G(\mathbf{r})&=\int\mu_0(\Delta\boldsymbol{\rho})\exp\left(-\frac{jk}{B}\mathbf{r}\cdot\Delta\boldsymbol{\rho}\right)\mathrm{d}^2\Delta\rho.\end{aligned}\tag{25}$$

If we drop the factor $G(\mathbf{r})$, Eq. (24) equals to the MCF of the fully developed field suggested by Eq. (8), which means that the influence of the surface roughness is reflected by the factor $G(\mathbf{r})$. The factor $G(\mathbf{r})$ is a Fourier transform of the complex coherence factor $\mu_0(\Delta\boldsymbol{\rho})$ of the rough surface. We assume the amplitude of the incident field is coarse compared with the surface structure, the complex coherence fact $\mu_0(\Delta\boldsymbol{\rho})$ of the reflected field can be found in the papers of Goodman [4]:

$$\mu_0(\Delta\boldsymbol{\rho})=\exp\left\{-k^2h_{rms}^2\left[1-\exp\left(-\left|\Delta\boldsymbol{\rho}\right|^2/l_c^2\right)\right]\right\},\tag{26}$$

where $k$ is the wave number. Equation (26) is derived assuming that the transmitted beam propagates vertically to the target surface. In order to analyze the effect of $\mu_0(\Delta\boldsymbol{\rho})$ to the receiving speckle distribution, Eq. (26) can be considered as being composed by two parts: a specular term $\exp(-k^2h_{rms}^2)$ and an exponentially attenuated term composed by the rest terms in Eq. (26). If $\Delta\mathbf{r}$ is chosen to be zero, the mutual coherence function $J(\mathbf{r},0)$ means the average intensity distributions of the speckle. If the speckles are fully developed, the function $J(\mathbf{r},0)$ is not affected by the coordinate position $\mathbf{r}=(x,y)$ in the receiving plane. However, for slightly rough cases, the function $J(\mathbf{r},0)$ is determined by the function $G(\mathbf{r})$, thus determined by $\mu_0(\Delta\boldsymbol{\rho})$.

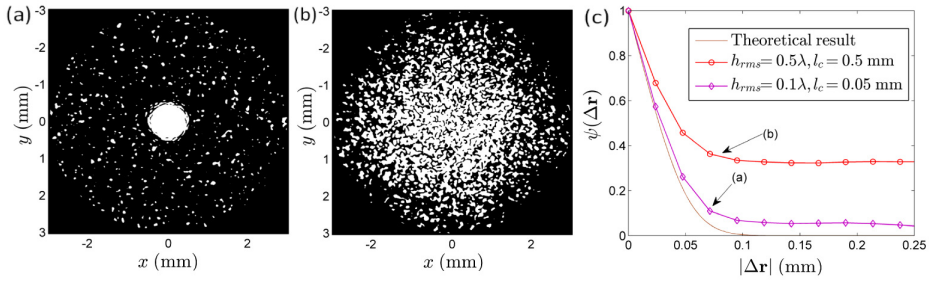


Fig. 6. (a) The central bright spot caused by the specular reflection of the slightly rough surface. (b) The non-uniform distribution of the average speckle intensity produced by the slightly rough surface. (c) The CSA functions for the two kinds of intensity distributions in (a) and (b) respectively, and the deviations introduced by the slightly rough surfaces can be found by comparing with the theoretical result.

The effects of the slightly rough surface for the speckle intensity distribution are shown in Fig. 6(a) and 6(b) using the simulation method and parameters given in Section 3.1. The deviations of the CSA functions $\psi(\Delta\mathbf{r})$ corresponding the speckles distributions in Fig. 6(a) and 6(b) are shown in Fig. 6(c). The slightly rough surface could affect the CSA function calculation.

#232043 - $15.00 USD Received 8 Jan 2015; revised 28 Feb 2015; accepted 1 Mar 2015; published 12 Mar 2015

The central bright spot shown in Fig. 6(a) can be explained by the specular term. As we has shown in Eq. (26), if $h_{rms}$ is small, the reflective speckle field has nonzero degree of coherence in the whole reflective area of the target plane, and only a small part of energy of the field is randomly reflected by the target to form the speckle pattern, while most of the energy of the field returns to the observation plane obeying the principle of specular reflection and forms a central bright spot in the intermediate plane. Based on Eq. (26), we can find that the specular term is completely determined by the surface roughness $h_{rms}$. If the value of $h_{rms}$ is greater than $0.4\lambda$, the specular term is nearly zero and consequently can barely affect the CSA function.

Figure 6(b) demonstrates the non-uniform distribution of the average speckle intensity caused by the slightly rough surface. This phenomenon affects the CSA function in a very complex way, and is related to many factors, such as $h_{rms}$, $l_c$ and the image aperture $\phi_{imag}$ of the observation system. Giving an exact criterion for this effect is difficult, unless some approximate methods are used. The first step is to define a new normalized correlation function by subtract the specular term out of Eq. (26), which is

$$\mu_1(\Delta\rho) = \frac{\mu_0(\Delta\rho) - \exp\left(-k^2 h_{rms}^2\right)}{1 - \exp\left(-k^2 h_{rms}^2\right)}, \tag{27}$$

We can remove the effects of the specular term by this operation. It is useful to define a coherence area of the non-specular term for the reflected wave. The square radius of the coherence area is:

$$\omega_e^2 = 2\int_0^\infty \rho \left|\mu_1(\rho)\right| d\rho \sim l_c^2 \Big/ \left(k^2 h_{rms}^2\right). \tag{28}$$

The last term in Eq. (28) is an asymptotic expression of this integral when the value of $h_{rms}$ is large enough [4]. The discussion about the specular term tells that the value of $h_{rms}$ must be larger than $0.4\lambda$, which could make this asymptotic expression to be valid with only small error. As shown in Eq. (25), when $\omega_e$ is small, the function $G(\mathbf{r})$ is a broad function of $\mathbf{r}$, thus the change of the average intensity in the observation aperture is hardly to be sensed. However, when $\omega_e$ is relatively large, the width of the function $G(\mathbf{r})$ may decrease, which causes the effect in Fig. 6(b). To simplify the problem, we use a Gaussian function whose waist equals to $\omega_e$ to take the place of Eq. (27). Taking this Gaussian function into Eq. (25), the half-width of the result function $G(\mathbf{r})$ approximately equals to $\lambda B/(\pi\omega_e)$ based on the Fourier transform result of a Gaussian function. Applying Eq. (28), the half-width of $G(\mathbf{r})$ is finally obtained to be $2|B|h_{rms}/l_c$. Numerical simulation proves that the error introduced by the non-uniform average intensities is unnoticeable when the half-width of $G(\mathbf{r})$ is larger than $\phi_{imag}/2$, which gives that $l_c < 4|B|h_{rms}/\phi_{imag}$. Together with the condition $h_{rms} > 0.4\lambda$, these conditions are the requirements of the surface roughness for the CSA metric. Using the parameters given in Section 3.1, our simulation requires that $h_{rms} > 0.21$ μm and $l_c < 114$ μm, and this result has been proved to be correct by simulations.

### *3.4 Metric performance and finite-sample effect*

Based on Eq. (9), the average speckle size is larger when the focusing spot size becomes smaller, which means there are fewer speckles inside the aperture of the observation system. And this would cause insufficient sampling and then large standard deviations of the estimated autocorrelation function. We name this phenomenon the finite-sample effect because this would not happen if our sample series is infinitely long, which is impossible in practical applications. Many factors can affect the finite-sample effect, such as the focusing spot size, the receiver aperture size, the focal length of the observation system and the pixel number and size of the sensor. The finite-sample effect introduces the most dominating error to the CSA metric when the focusing spot size is small. Thus we will analysis the finite-

#232043 - $15.00 USD Received 8 Jan 2015; revised 28 Feb 2015; accepted 1 Mar 2015; published 12 Mar 2015

sample effect by simulation and put forward a method to evaluate error it introduced to the CSA metric in this section.

Figure 7 illustrates the metric $M_e$ as a function of the laser focusing spot size $\omega_0$. We choose the clipped autocorrelation value $\psi(\Delta\mathbf{r})$ to be 0.5 here. The simulation result is given by the method and the system parameters in Section 3.1, while the theoretical result is calculated by Eq. (16) using the same system parameters. The simulation is completely consistent with the theoretical result when the focusing spot size $\omega_0$ is large enough. However, when the focusing spot becomes smaller, the simulation result deviates from the theoretical one, which is proved to be caused by the finite-sample effect. Besides the finite-sample effect, the invalidity of the circular Gaussian assumption used in Eq. (2) also introduces error to the model of the metric $M_e$ when the value of $\omega_0$ is very small. However, the instability of the metric caused by the finite-sample effect always dominates the error unless the focusing spot size has nearly the same magnitude as the autocorrelation of the rough surface. We do not discuss the error introduced by the circular Gaussian assumption here, because the metric has already unavailable if the focusing spot size becomes such small.

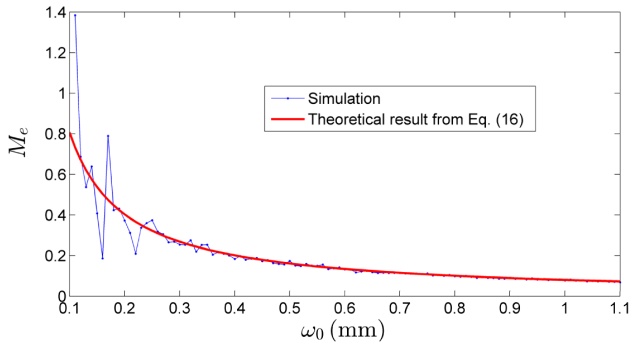


Fig. 7. The CSA metric is shown as a function of the focusing spot size $\omega_0$. The simulation results are calculated by the parameters in Section 3.1 and the theoretical result for comparing is calculated by Eq. (16).

The variances of the estimated autocorrelation function are investigated by Bartlett [12], which can be expressed as:

$$\operatorname{var}\{\hat{\psi}(s)\} \sim \frac{1}{N}\sum_{m=-\infty}^{\infty}[\psi^2(m)+\psi(m+s)\psi(m-s) + 2\psi^2(s)\psi^2(m)-4\psi(s)\psi(m)\psi(m-s)+\kappa_4(m,s,0)]. \tag{29}$$

The estimated autocorrelation function is denoted by $\hat{\psi}$, and $\kappa_4$ stands for the fourth order cumulant. The parameter $N$ is the sampling number, and the variable $s$ and $m$ are integers which represent the counts of the sample points of the speckle pattern. Equation (29) is an approximate expression of the variance of the estimated autocorrelation function. Equation (29) is derived for the one dimensional data, which is not suitable for the two dimensional cases, for instance the CSA case here. In order to generalize Eq. (29) to two dimensional cases, we introduce a concept of effective sample number of the speckle pattern. The effective sample number is given as:

$$N' = \frac{N^2}{\sum_i\sum_j \psi\left(\left|r_i - r_j\right|\right)} = \frac{N^2}{N+2\sum_{k=1}^{N-1}(N-k)\psi(k)} \tag{30}$$

The meaning of Eq. (30) can be explained as follows: The $N \times N$ matrix composed by the data of the speckle distribution is treated as $N$ different one-dimensional sequences which all have the sampling number of $N$. The $N$ different one-dimensional sequences are not independent,

#232043 - $15.00 USD Received 8 Jan 2015; revised 28 Feb 2015; accepted 1 Mar 2015; published 12 Mar 2015

but have the correlations described by $\psi(\Delta r)$, and that is why we divide $N^2$ by the sum of the autocorrelation function $\psi(\Delta r)$. By replacing the parameter $N$ with $N'$ in Eq. (29), we transform the two-dimensional case into a one-dimensional one.

If the stochastic process is a general linear process, then the fourth order cumulant $\kappa_4$ is zero. But the stochastic process generated by the clipped speckle pattern is not general linear, which may result in a nonzero $\kappa_4$. Some exploration shows that the fourth order cumulant is very small compared with the other terms in Eq. (29), which means we can omit the term $\kappa_4(m,s,0)$ without losing much accuracy of Eq. (29). This helps to save much calculation time. Using the system parameters given in Section 3.1, we calculate the deviation of the metric $M_e$ in Fig. 8 for two different focusing spot size without the cumulant $\kappa_4$. The simulations are given for one hundred different realizations of the diffuse targets. The simulation results prove that omitting the fourth order cumulant $\kappa_4(m,s,0)$ do not affect much of the accuracy of Eq. (29), because nearly all the $M_e$ results of the one hundred simulations located in the range predicted by Eq. (29). In Fig. 8, the mean values calculated by Eq. (16) are not identical to the mean values of the simulations, and this bias can be explained by the fitting error illustrated by Fig. 5, which is too small to have a significant effect to the metric. After proving the correctness of Eq. (29), we are going to explore its influence on the performance of this metric.

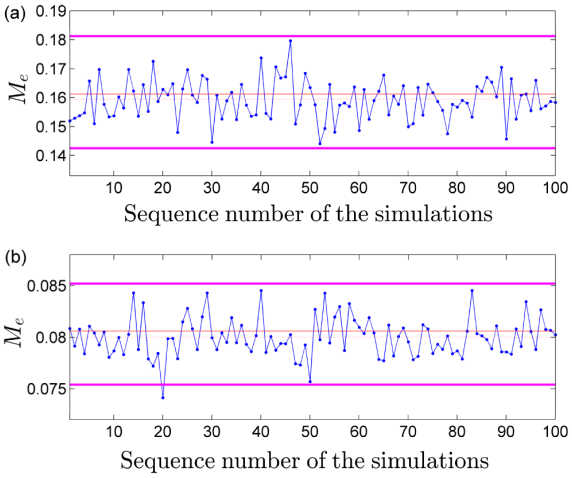


Fig. 8. The simulations of the CSA metric $M_e$ using one hundred different realizations of the diffuse target. Every point in this figure stands for a simulation result. The thick lines on the top and bottom are the deviations calculated by Eq. (29). The solid and dot lines in the center are the mean values of the theory Eq. (16) and the simulation respectively. The focusing spot sizes are (a) 0.5 mm and (b) 1.0 mm.

#232043 - $15.00 USD Received 8 Jan 2015; revised 28 Feb 2015; accepted 1 Mar 2015; published 12 Mar 2015

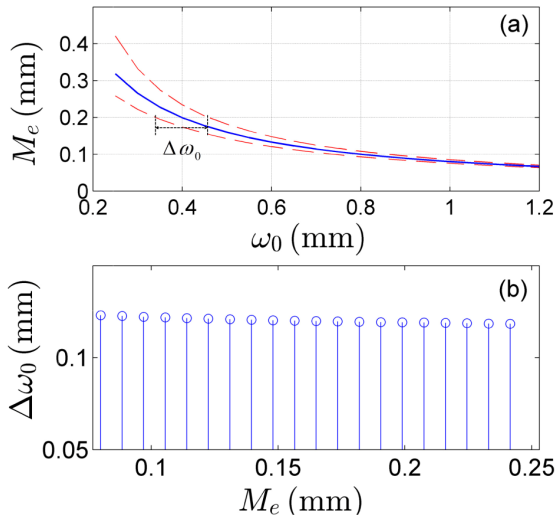


Fig. 9. (a) The deviation range of the CSA metric calculated by Eq. (29) and Eq. (30). The dash lines are the upper and lower boundary of the range. (b) The accuracy $\Delta\omega_0$ of the metric changes against the value of $M_e$.

The deviation range of the CSA metric, which is caused by the finite sample effect, is shown in Fig. 9(a) for different sizes of the beam focusing spot $\omega_0$. The dash lines in Fig. 9(a) represent the upper and the lower boundaries of the metric deviation. The result given in Fig. 9(a) is consistent with the simulations given in Fig. 7, and completely explains the reason of the deviation of the simulations from the theoretical result. When the focusing spot size $\omega_0$ decreases, the range of the deviation becomes large. If there is a focusing spot on a remote target, we cannot determine the focusing spot size is 0.40 mm or 0.43 mm base on this CSA metric, because the metrics of 0.40 mm and 0.43 mm have an overlap section of the deviation range. But we can make sure that the focusing spot size is not 0.6 mm for there are no overlaps of these deviation ranges. Therefore we can define the accuracy of the metric as the minimum change of the laser focusing spot whose deviation ranges of $M_e$ are not overlapped. It can be found that the deviation ranges do not have overlaps only when both the upper boundary and the lower boundary have the same values of $M_e$, so the difference of the focusing spot sizes satisfying this condition, which is noted as $\Delta\omega_0$ in Fig. 9(a), can be defined as a measurement of the accuracy of the metric. Applying the numerical method, we calculate the values of $\Delta\omega_0$ for different metric $M_e$ values, which is demonstrated in Fig. 9(b). An important conclusion can be drawn from this simulation result: Although there is a small decline, the values of $\Delta\omega_0$ do not change obviously with the metric values or the focusing spot size, and nearly remain to be a constant of 0.12. It means that the metric $M_e$ cannot tell the difference of the focusing spot size precisely if the change of the focusing spot is smaller than 0.12 mm.

### *3.5 Comparison with the direct observation method*

In most laser beam focusing systems, the observation systems are designed to image the far-distant focusing spots directly using objective lens and cameras, and then the change of the focusing spot size is derived from the change of the image spot size. This method can provide the dimensional information of the spot directly, and do not need complicated signal processing system for subsequent processing. However it also has natural limitations from the pixel size of the camera and the F-number of the objective lens.

In order to compare the direct observation method with the CSA method, we use the same observation system given in Section 3.1. Since the speckle image size $\phi_{imag}$ is 6 mm and the sampling number $N$ is 1024, the pixel size in the image plane can be calculated to be 5.8 μm. The object distance $z$ is the sum of $z_1$ and $z_2$ in Fig. 4, which is 10.2 m. Based on the image

#232043 - $15.00 USD Received 8 Jan 2015; revised 28 Feb 2015; accepted 1 Mar 2015; published 12 Mar 2015

geometry of a lens with a focal length of 200 mm, the image spot size is 1/51 times the focusing spot size on the target. The minimum change of the image spot size which can be sensed by the detector is equal to the pixel size 5.8 μm. As a result, the minimum change of the focusing spot size can be detected is about 5.8 μm × 51 ≈0.3 mm. Some sub-pixel algorithm could be used to make the change of the spot size smaller than this size detected. But all the sub-pixel algorithms have a common precondition that the image of the target need to be composed of enough number of pixels. In our paper, when the focusing spot size is nearly 0.6 mm, the image of the spot contains at most four pixels with an optical system whose focal length is 200 mm, and the sub-pixel algorithms are not available as far as we know.

According to the simulations in Section 3.4, the accuracy of the metric $M_e$ is about 0.12 mm, which is smaller than the 0.3 mm of the direct method. Consequently, we can conclude that the metric of the clipped speckle autocorrelation method is more accurate than the direct method when the focusing spot size becomes very small. However, the slope of the metric becomes smaller when the focusing spot becomes large and the change of $M_e$ could be hard to detect. This difficulty would not happen when the direct method is used. And when the focusing spot size is large, sub-pixel algorithm could be used, which makes the direct observation method more advantageous in this situation.

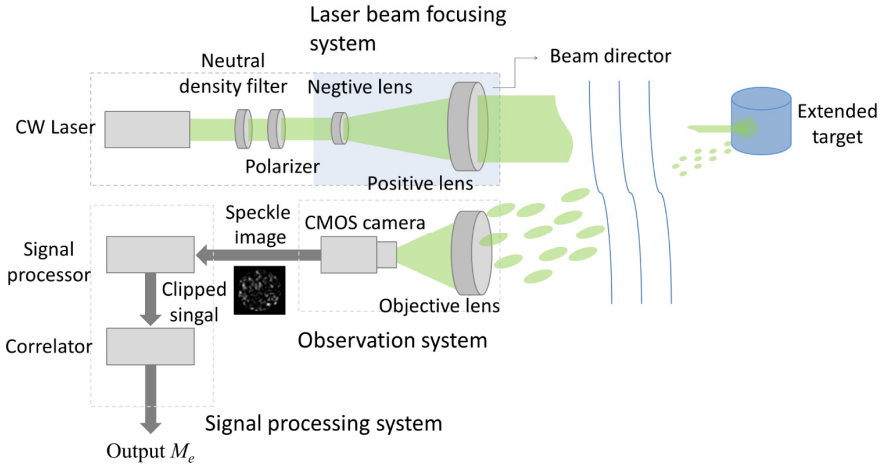


Fig. 10. The experimental setup for examining the CSA metric and its performance.

## 4. Experiment

The experiment is managed according to the arrangements of the optical apparatuses shown in Fig. 10. There are three major systems playing important roles, which are the laser beam focusing system, the observation system and the signal processing system. In the laser beam focusing system, we focus a CW (continues wave) laser with wavelength of 0.532 μm to an extended target. The speckles generated by the rough surface of the target are detected by an objective lens with a focal length of 200 mm and a CMOS camera with the pixel size of 4.7 μm in the observation system. The observation system collects the returned speckle field and generates an image of the speckle distribution using the configuration discussed in Fig. 6. The F-number of the observation objective lens is 10, thus the entrance pupil diameter is 20 mm. The distance from the target to the objective lens of the observation system is 8.4 m. After the speckle images are obtained from the observation system, we can calculate the diameter of the image size on the CMOS detector, which turns out to be 5 mm. Taking the parameters given above into Eq. (20), the magnifying power $A_{im}$ is derived to be –0.28 and $z_1$ to be 7.48 m. The last system, which is called the signal processing system, treats the speckle images as input signals, and then exports the final metric $M_e$ of the whole system. The threshold

#232043 - $15.00 USD Received 8 Jan 2015; revised 28 Feb 2015; accepted 1 Mar 2015; published 12 Mar 2015

parameter $b$ is set to be 1.8 to eliminate the back ground noise. Since the speckle images also suffer some residual noise from the observation system, the signal processor processes the images with a Gaussian filter and then changes the speckle images into one-dimensional binary signals of 0 and 1. A correlator is used to do the autocorrelation process and then calculate the metric $M_e$.

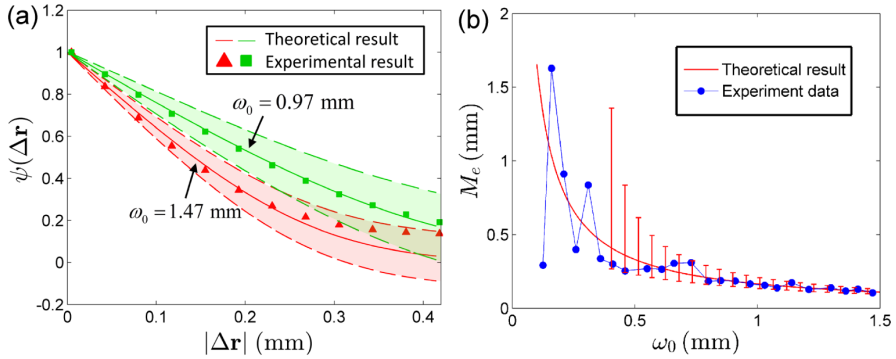


Fig. 11. (a) The CSA function derived from experimental data. The areas between the dash lines stand for the deviation range predicted by Eq. (29). (b) The experimental result for CSA metric Me. The error bars are the deviation ranges for the corresponding spot size.

The autocorrelation result of the clipped speckle signal is shown in Fig. 11(a), where the markers stand for the experimental results, the solid lines the theoretical results, and the areas between the dash lines are the deviation ranges caused by the finite sample effect calculated by Eq. (29) and Eq. (30). We show two different focusing spot sizes of 0.97 mm and 1.47 mm in Fig. 11(a). The clipped autocorrelation functions derived from the experimental data locates in the deviation ranges predicted by Eq. (29), therefore the theoretical considerations are proved to be correct by the experiment. Notice that the deviation ranges just have no overlaps with each other when autocorrelation functions are about 0.5, which suggests that the accuracy of the metric $M_e$ for this situation is about $\Delta\omega_0$ = 1.47-0.97 = 0.5 mm. This accuracy of the metric is much bigger than the simulation result of 0.12 mm given in Section 3.4. The explanation accounting for the large value of the accuracy of the experiment could be the observation lens with a small aperture used in the experiment. For the same detection distances and the same focal lengths of the observation systems, a smaller aperture size means fewer speckles in the speckle images, and this aggravates the finite sample effect, furthermore, causes the increase of the deviation ranges, which makes the metric less accurate here. If we need the metric to be stable with very small fluctuation, then an observation system with a small F-number should be considered.

Figure 11(b) shows a group of $M_e$ values changing with the focusing spot radius $\omega_0$. The metric is calculated when $\psi(\Delta\mathbf{r}) = 0.6$. The solid line is the theoretical result given by Eq. (16) using the parameters of the apparatus in Fig. 10. The error bars indicate the deviation ranges of metric for the corresponding focusing spot sizes. It can be found that the error bars become longer with the increasing of the focusing spot sizes, which is consistent with both the theoretical predictions and the simulations discussed above. When the focusing spot radius $\omega_0$ is smaller than 0.4 mm, the lengths of the error bars become so long that it is not convenient to be shown in Fig. 11(b), hence in this range, the metric $M_e$ loses its stability. Although not all of the experimental data lie on the theoretical curve exactly, they remain to be located in the predicted range of the deviation, which proves the correctness of our analysis.

## 5. Conclusion

The metric based on the clipped speckle autocorrelation (CSA) method is developed to increase the beam energy concentration on a diffuse target for a laser beam projection system. The quality of the metric determines the final optimization result of a model free optimization

#232043 - $15.00 USD Received 8 Jan 2015; revised 28 Feb 2015; accepted 1 Mar 2015; published 12 Mar 2015

algorithm, such as SPGD. However, the quality of the speckle-based metric for the beam energy concentration has been seldom discussed in the past. Hence the performance of the CSA metric is analyzed for many influencing factors by the simulation method in this paper.

The second order statistics of the fully developed speckle which are the basis for the speckle autocorrelation have been reviewed for completeness. Using this preliminary theory and the relation of the clipped and unclipped autocorrelation function, we derive the analytical expression for the CSA metric with the help of the curve fitting technique. The CSA metric is defined as the lag length for a certain value of the clipped autocorrelation function. For a particular value of the clipped autocorrelation function, the focusing spot size is inversely proportional to the lag length or the CSA metric value. In the simulation, the diffuse target is modeled using a digital filter method where we can change the RMS height and the correlation length of the rough surface. The field propagation task is accomplished by the FFT-based algorithm. For the autocorrelation calculation in the simulation, we applied the spatial average instead of the ensemble average which brings much convenience. Based on these simulation techniques, we analyze the influence of the surface roughness on the metric accuracy and conclude that the RMS height $h_{rms}>0.4\lambda$ and the correlation length of the surface $l_c<4|B|h_{rms}/\phi_{imag}$. These surface conditions are not strong for most of the non-specular surface, and define the extent of the application situation for our metric. According to the simulation result, the metric performance is mainly limited by the finite sample effect when the size of the focusing spot size is small. If the focusing spot size is small, the speckle size becomes large and as a result, the speckle number in the observation aperture tends to be one. This would cause the metric extremely unstable and the deviation generated by this unstable environment can be predicted using Eq. (29) and Eq. (30). The accuracy of the metric is defined to qualify the uncertainty of the CSA metric considering the influence of the finite sample effect. Finally, an experiment is designed for testing the discussions for the metric performance. The experiment examines the validity of this CSA metric and proves the correctness of the analysis of the metric performance. Comparing with the simulation condition, we can find that the way to suppress the finite sample effect and enhance the metric stability is to reduce the F-number or increase the aperture size of the observation system.

**Acknowledgments**

This work is funded by the State Key Laboratory Foundation of Laser Interaction with Matter of China.

#232043 - $15.00 USD Received 8 Jan 2015; revised 28 Feb 2015; accepted 1 Mar 2015; published 12 Mar 2015